Geophys. J. Int. (1997) **128**, 285–300

Seismic properties of layer 2 basalts

Joel E. Johnston* and Nikolas I. Christensen
Purdue University, Department of Earth and Atmospheric Sciences, West Lafayette, IN 49707, *USA*

Accepted 1996 August 27. Received 1996 August 19; in original form 1995 October 2

SUMMARY

In this paper the physical properties of oceanic layer 2 basalts are examined with the emphasis on microcrack porosity and alteration-related changes in physical properties. Over 160 core samples from some of the more significant Deep Sea Drilling Project/Ocean Drilling Program holes, including 417D, 418A, 504B and 801C are included in the present investigation. Overall physical property relationships are discussed in the first half of this study. At 200 MPa confining pressure, compressional- and shear-wave velocities of the sample suite have modal values of 6.1 kms^{-1} and 3.5 kms^{-1}, respectively. A Poisson's ratio of 0.28 characterizes the majority of the basalts. Samples that have experienced extensive low-temperature alteration, identified through elevated K_2O and decreased CaO and MgO contents, exhibit low velocities (and densities) and high Poisson's ratios.

The microcrack porosity in the basalt suite is examined using velocity–pressure data, a pore-aspect-ratio inversion scheme, and scanning electron microscope (SEM) imaging. Microcracks sealed by alteration minerals such as smectite and calcite or healed by late crystallization are common throughout the sample set. Rocks from the transition zone and sheeted dyke section of Hole 504B are marked by numerous smectite- and chlorite-filled cracks. More significantly, the data indicate an increase of low-aspect-ratio open microcracks with increasing depth in samples from several DSDP holes, particularly Hole 504B. These microcracks, also observed using the SEM, are attributed to stress relief as the original drill cores were removed from *in situ* pressure conditions. Stress-relief microcracking is apparently more severe in the holocrystalline, coarser-grained samples from massive flows than in the phyric basalts with fine-grained groundmasses characteristic of pillow units. This difference in microcracking is explained through basic fracture theory

Key words: igneous rock, layer 2, microcracks, Poisson's ratio, porosity, seismic velocities.

INTRODUCTION

Since the first recovery of oceanic basalt in 1968 during Leg 2 of the Deep Sea Drilling Project, the physical properties, particularly seismic velocities, of layer 2 rocks have been investigated in many studies dealing with both dredge-haul and drill-core samples (e.g. Christensen 1972; Christensen & Salisbury 1972, 1973; Schreiber & Fox 1976; Wallick, Christensen & Ballotti 1990; Wilkens, Fryer & Karsten 1991). The interest in seismic properties of layer 2 basalts can be traced to the fact that both seismic refraction profiles and laboratory studies have identified age- (and depth-) dependent changes in physical properties of this layer. Specifically, seismic refraction studies indicate a relatively rapid increase in velocity with both age and depth of the upper portion of layer 2 (Houtz & Ewing 1976; Ewing & Purdy 1982; Vera & Mutter 1988; Jacobsen 1992). This increase in velocity has been attributed primarily to the sealing of large- and small-scale porosity by hydrothermal minerals (e.g. Houtz & Ewing 1976; Wilkens *et al.* 1991). In contrast to the seismic refraction findings, early laboratory studies of layer 2 basalt cores identified a decrease of both seismic velocity and density with increasing age caused by the effects of low-temperature alteration (e.g. Christensen & Salisbury 1972, 1973; Salisbury & Christensen 1973; Hart 1973).

Additional studies have focused on the evolutionary aspects of layer 2 or have further explored physical properties relationships in these basalts. Christensen & Salisbury (1975) summarized velocity–density systematics of layer 2 basalts in a paper

* Now at: Exxon Exploration Company, PO Box 146, Houston, TX 77001-0146, USA.

dealing with the composition of the lower oceanic crust. Schreiber & Fox (1976) examined dredge basalts from the Oceanographer fracture zone and found that variations in sample porosity and pore aspect ratio exert a stronger control on measured velocities than mineralogy. Hyndman (1979) reviewed existing laboratory and field Poisson's ratio data for the upper oceanic crust and concluded that the Poisson's ratio of layer 2 increases with increasing low-temperature weathering, hydrothermal alteration and porosity. Christensen (1984) examined the effects of pore pressure on V_p, V_s and Poisson's ratio of layer 2 basalts. It was demonstrated that elevated pore pressures could in part be responsible for low velocities and high Poisson's ratios for upper layer 2. Carlson & Herrick (1990) used logging results from DSDP Holes 395A and 418A, and laboratory core physical property measurements to examine changes in porosity, density and compressional-wave velocity in the upper oceanic crust as a function of depth and age. They concluded that the velocity structure of the upper oceanic crust is controlled by changes in porosity and alteration (and metamorphic grade), rather than by igneous structure. Recently, Wilkens *et al.* (1991) used laboratory measurements, ophiolite outcrop observations, logging data and velocity–porosity theory to examine porosity and pore aspect ratios of the upper oceanic crust as a function of age and depth. It was shown that the sealing of relatively thin (low-aspect-ratio) cracks with hydrothermal minerals could explain the observed large increase of layer 2a velocity with age, without necessarily significantly decreasing overall layer 2a porosity. Finally, Jacobsen (1992) reviewed previous studies dealing with the seismic properties of upper layer 2 and produced a qualitative model of layer 2a crustal evolution to explain the observed increase in seismic velocities with age. The interested reader is also referred to Christensen 1970; Christensen & Shaw 1970; Christensen 1972; Christensen, Fountain & Stewart 1973; Fox, Schreiber & Peterson 1973; Hyndman & Drury 1976; Salisbury *et al.* 1988; Moos, Pezard & Lovell 1990; Berge, Fryer & Wilkens 1992; Johnson & Semyan 1994; and the Deep Sea Drilling Project/Ocean Drilling Program literature in general.

Although the list of publications dealing with oceanic layer 2 is quite extensive, a considerable need exists for a comprehensive study of the physical properties of layer 2 basalts obtained during the past two decades of the Deep Sea Drilling Project/Ocean Drilling Program. In the present study the velocities, porosities, densities and mineralogies of over 160 basalt samples from several well-known DSDP/ODP holes (including 417D, 418A, 504B and 801C) are examined in detail using laboratory velocity measurements as a function of confining pressure, a pore-aspect-ratio inversion program, scanning electron microscope (SEM) imaging and geochemical analyses. The primary goals of this study are to investigate possible systematic changes in microcrack porosity with depth in the sample suite, as well as to constrain further alteration-induced changes in the physical properties of layer 2 basalts using a relatively large number of samples.

DSDP/ODP SAMPLES AND EXPERIMENTAL TECHNIQUES

Samples from 12 separate DSDP/ODP drillholes sampling upper oceanic crust ranging in age from approximately 3 Ma to 160 Ma were examined in the present study (Fig. 1, Table 1). Ocean Drilling Program site 801, located in the 'Jurassic quiet zone' of the Pacific, recovered both normal mid-ocean-ridge- and alkali ocean-island-type basalts ranging in condition from fresh to extremely altered (Lancelot *et al.* 1990; Floyd & Castillo 1992). At 160 Myr old, basalt cores from this site represent the oldest oceanic crust yet recovered during DSDP/ODP operations (Lancelot *et al.* 1990). Holes 417A, 417D and 418A were drilled during DSDP legs 51–53. These drillholes were located on Atlantic oceanic crust approximately 110 Myr old. Hole 417A reached 417 m below the seafloor (mbsf), penetrating 209 m into basalt basement comprised of highly altered pillows and a relatively fresh massive flow unit. Hole 417D, located 500 m away from 417A, penetrated 365 m into basalt basement consisting mainly of pillows and interdispersed basalt breccias and massive flow units. Hole 418A extended 544 m into basalt basement, intersecting massive units at the top and bottom of this interval with mainly pillow basalts between. In contrast to Hole 417A, the basalts cores taken from 417D and 418A for the most part exhibit only weak to moderate alteration (Donnelly *et al.* 1980).

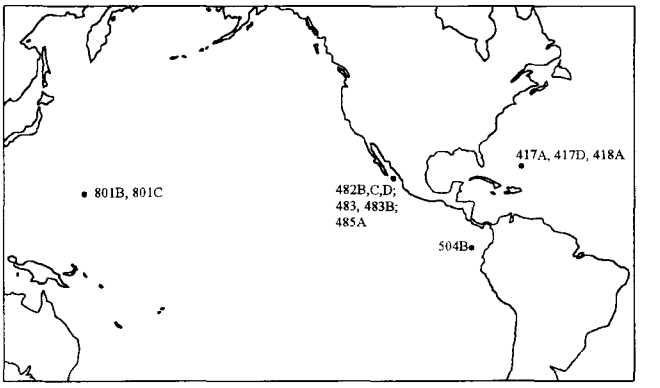

Figure 1. Location of DSDP/ODP holes examined in this study.

Hole 504B was started in 6 Myr old Pacific oceanic crust south of the Costa Rica Rift during DSDP leg 69. In the present study, samples collected during legs 69, 70 and 83 were examined. By the end of leg 83, Hole 504B had penetrated 1075 m into basalt basement and extended through the entire extrusive volcanic pile into a zone of sheeted dykes and massive units of what is believed to be seismic layer 2c (Cann *et al.* 1983; Anderson *et al.* 1985). To a depth of ~850 mbsf, the basalts were found to have experienced primarily low-temperature alteration. At approximately 850 mbsf and below, in the transition zone between the pillow basalts and the sheeted dyke/massive basalt units, the presence of greenschist facies alteration was identified. The boundary between seismic layers 2b and 2c was placed at approximately 850 mbsf (Anderson *et al.* 1985). Relatively young basalts (<3 Ma) were also examined from sites 482, 483 and 485 located in the Gulf of California (Lewis *et al.* 1983) during Leg 65. In general, fresh pillow basalt and massive basalt units were found interlayered with sediments at each of these locations.

Prior to velocity measurements, lengths, diameters and weights of the cores were determined before copper jackets were applied to the samples to exclude pressure fluid. The samples were then 'seasoned' by cycling the cores to confining pressures in excess of 200 MPa (without measuring velocities) to remove the effects (if any) of hysteresis on the ensuing velocity–pressure runs. Compressional- and shear-wave velocities of the basalts were then measured to 200 MPa under both

Table 1. DSDP/ODP drillhole data including ages, borehole depths and number of samples studied per hole.

Hole	Leg	Location	Approx. Age (Ma)	Water Depth (m)	Sediment Thickness (m)	Basement Penetration (m)	No. Samples
417A	51-53	Atlantic, Bermuda Rise	110	5468	208	209	14
417D	" "	" "	" "	5482	343	365	29
418A	" "	" "	" "	5510	324	544	46
482B-D, 483, 483B, 485A	65	Pacific, Gulf of California	< 3	3000 to 3084	110 to 150	47 to 177	31
504B	69,70,83	Pacific, Costa Rica R.	6	3470	275	1075	26
801B	129	Pacific, Pigafetta Basin	160	5674	462	50	4
801C	" "	" "	" "	5674	494	100	16
						total:	166

water-saturated and unsaturated conditions using an extremely accurate (to within ± 0.5 MPa) Heise pressure gauge. Velocities were measured using the pulse transmission technique (Christensen 1985) and 1 MHz dominant frequency compressional and shear transducers. Prior to the saturated runs, the cores were vacuum-saturated for one month and their weights measured again. After wrapping the samples in copper mesh to allow for the expulsion of pore fluid (thus keeping pore pressures near atmospheric), new jackets were applied to the cores and their saturated velocities were measured. Using sample volumes and saturated and dry weights, the dry bulk densities, wet bulk densities and effective porosities of each sample were calculated.

PHYSICAL PROPERTIES

Histograms of compressional- and shear-wave velocities of the basalts at 200 MPa under saturated conditions are shown in Fig. 2. Strong peaks in V_p and V_s are evident between 6.0 and 6.4 km s^{-1} and 3.3 and 3.6 km s^{-1}, respectively. The overall distribution of velocities is obviously skewed due to low-velocity altered basalts, particularly from 417A, 417D, 801B and 801C (e.g. Christensen & Salisbury 1972, 1973). In Fig. 3, compressional- and shear-wave velocities (saturated, 200 MPa) are plotted against the respective wet bulk densities. The basalts exhibit a wide range of densities (2.4 to 3.0 g cm^{-3}) from the most altered samples of holes 801B, 801C and 417A to the relatively fresh basalts taken from the lower portions of 418A and 504B. As might be expected, a good overall trend of increasing velocity with increasing wet bulk density is evident in Fig. 3. Poisson's ratios of the basalts are roughly centred around a value of 0.28 at 200 MPa, with more weathered samples having greater values, up to 0.35 for some of the Jurassic basalts of Hole 801C (Fig. 4). Some of the holocrystalline, relatively unweathered basalts/dolerites from the deeper portions of Hole 504B exhibit high Poisson's ratios as well, which may be related to the presence of high-temperature alteration minerals (see below). Lastly, compressional- and shear-wave velocities (saturated, 200 MPa) are plotted against sample porosities in Fig. 5. Note that the majority of the basalts have porosities of 5.0 per cent or less. A trend of decreasing velocity with increasing porosity is apparent, with scatter mainly due to mineralogy (alteration) and pore-aspect-ratio variations from sample to sample.

To explain fully the trends found in the velocity data presented above, whole rock geochemical analyses were obtained for a subset of the samples (32 in all), which spans

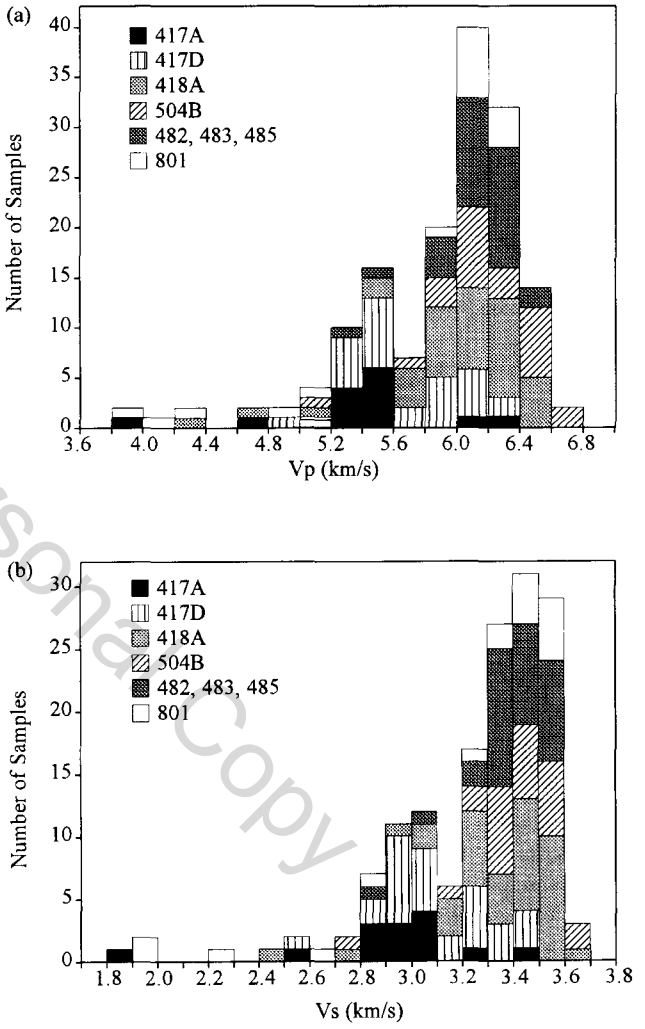

Figure 2. Compressional-(a) and shear-wave (b) velocities (200 MPa, saturated) of the basalt suite.

the range of physical property variations observed in this study (Table 2). Previous studies have shown that CaO, MgO and K_2O vary significantly with degree of alteration in layer 2 basalts (e.g. Hart 1973; Donnelly, Thompson & Robinson 1979); therefore, the following analysis is restricted to these oxides. The effects of composition on physical properties are isolated in most of the following figures by multiplying sample dry bulk densities by the weight per cent of each oxide to

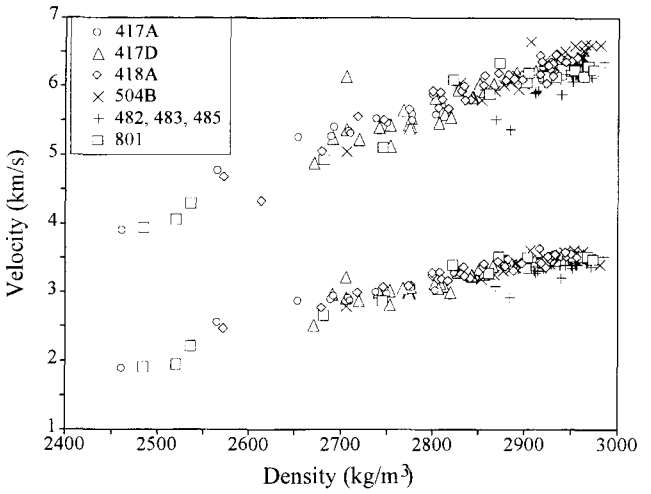

Figure 3. Compressional- and shear-wave velocities (200 MPa, saturated) versus wet bulk densities.

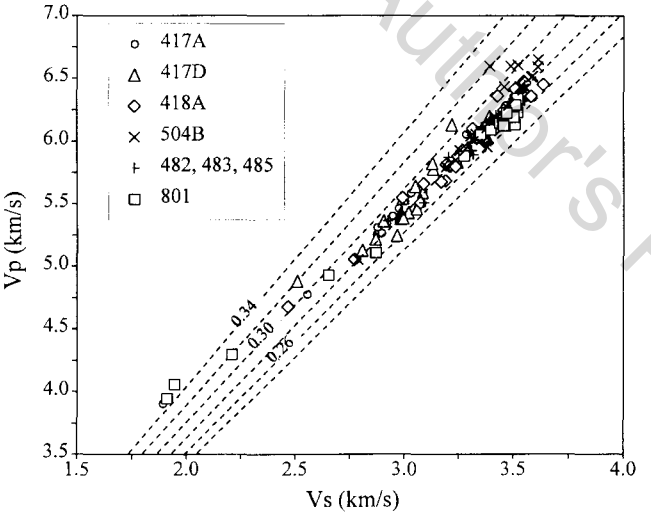

Figure 4. Compressional-wave velocity versus shear-wave velocity (200 MPa, saturated) with lines of constant Poisson's ratio.

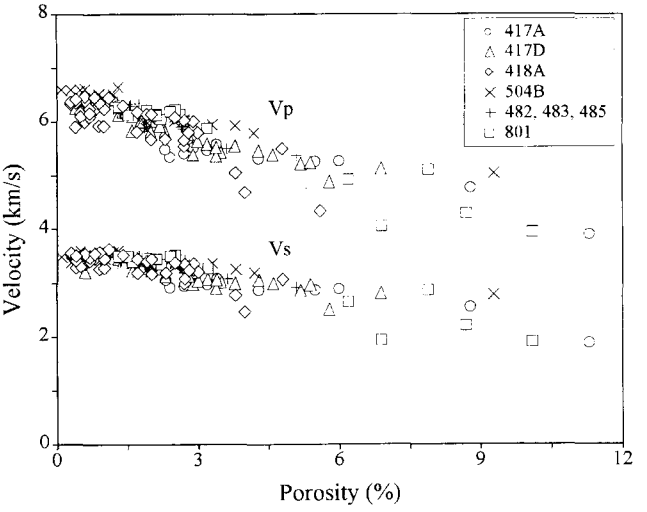

Figure 5. Compressional- and shear-wave velocities (200 MPa, saturated) versus porosity.

produce elemental abundances in mass per sample volume units. Mass/volume units are preferable because they represent the actual amount of element per sample volume (Hart 1973; Busch *et al.* 1992).

Grain densities of the basalts are observed to increase with increasing MgO and CaO content and to decrease with increasing K_2O (Fig. 6). In Fig. 7, compressional- and shear-wave velocities measured at 200 MPa (saturated) in the basalts have been plotted as a function of MgO, CaO and K_2O contents. High-pressure velocities were chosen for analysis to minimize the effects of microcracks on velocity; previous studies have dealt only with atmospheric pressure velocity measurements (e.g. Busch *et al.* 1992; Johnson & Semyan 1994). Velocities are found to increase with increasing CaO and MgO and to decrease with increasing K_2O, with high correlation coefficients for the least-squares line fits to these data (Fig. 7). Plots of Poisson's ratio at 200 MPa against MgO, CaO and K_2O contents present more scattered patterns (Fig. 8). Poisson's ratio appears to decrease with increasing MgO and CaO content, but with a significant number of outlying points (Figs 8a and b). More convincing is the trend of increasing Poisson's ratio with increasing K_2O (Fig. 8c).

The basalts listed in Table 2 have primarily experienced low-temperature alteration (i.e. <50–$100\,^{\circ}C$) (Donnelly *et al.* 1979; Alt & Honnorez 1984; Alt *et al.* 1986), which results in lowered grain densities and velocities, and elevated Poisson's ratios, relative to values for fresh basalts. Low-temperature alteration of plagioclase, pyroxene, olivine and glass to clay minerals (smectite, palagonite, etc.) results in a net loss of Ca and Mg to seawater (e.g. Hart 1970, 1973; Donnelly *et al.* 1979; Alt & Honnorez 1984; Alt *et al.* 1986). In contrast, potassium is taken up from seawater by layer 2 basalts during low-temperature alteration to produce K-rich clays (celadonite, palagonite, etc.) and K-feldspar (e.g. Hart, 1973; Alt & Honnorez 1984; Alt *et al.* 1986). Potassium content appears to be a particularly effective indicator of alteration; the velocity data are very well correlated with this parameter (Figs 7c and 8c). The highly altered basalts from holes 417A, 801B and 801C have significantly elevated K contents (up to 5.0 per cent) relative to the remaining samples from 417D, 418A and 504B (Table 2). Fresh layer 2 basalts typically have K_2O contents of much less than 1 per cent (e.g. Donnelly *et al.* 1979). As might be expected, alteration as identified by K_2O content is most severe in higher-porosity basalts (Fig. 9). The degree of sample alteration thus has a very significant influence on the velocity–porosity trends shown in Fig. 5 (e.g. Carlson & Herrick 1990).

Figs 6–9 emphasize the important effects of low-temperature alteration on the physical properties of layer 2 basalts, first discussed by Christensen & Salisbury (1972, 1973), Hart (1973) and Hyndman (1979). It should be mentioned here that four of the deepest Hole 504B samples included in the geochemistry data set, taken from the transition zone and below, probably experienced much higher hydrothermal alteration temperatures (upwards of 300 °C, Alt *et al.* 1986), which can result in geochemical changes differing from those experienced in the low-temperature regime (e.g. Alt *et al.* 1986). For example, samples 504B-127-1 and 504B-136-1, which have Poisson's ratios above 0.30, also have relatively high MgO contents (Table 2, Fig. 8a), which are probably due to the presence of chlorite and amphibole (Alt *et al.* 1986).

Table 2. Chemical analyses (oxides in weight percent) and physical property data for selected samples including bulk densities (ρ), porosities (ϕ), saturated velocities at 200 MPa and Poisson's ratios (σ).

Sample	SiO_2	Al_2O_3	Fe_2O_3*	MgO	CaO	Na_2O	K_2O	TiO_2	P_2O_5	MnO	Cr_2O_3	LOI	Sum	ρ dry (g/cm^3)	ρ wet (g/cm^3)	ϕ (%)	Vp (km/s)	Vs (km/s)	σ
417A-24-1	49.40	18.22	9.55	3.17	2.77	1.39	4.96	1.72	0.13	0.14	0.04	8.80	100.3	2.349	2.461	11.3	3.903	1.892	0.35
417A-27-1	46.85	17.29	10.78	5.07	9.36	1.99	1.96	1.43	0.22	0.15	0.03	5.00	100.1	2.683	2.708	2.4	5.346	2.919	0.29
417A-33-5	46.64	16.77	10.17	4.73	10.88	2.16	1.53	1.49	0.17	0.13	0.04	5.80	100.5	2.630	2.689	6.0	5.271	2.897	0.28
417A-46-4	45.91	17.87	8.17	5.58	11.36	2.12	1.05	1.42	0.13	0.10	0.04	6.30	100.0	2.665	2.692	2.7	5.408	2.947	0.29
417D-22-1	48.21	15.87	10.61	6.15	11.60	2.27	0.44	1.39	0.10	0.17	0.04	3.40	100.2	2.668	2.720	5.2	5.221	2.869	0.28
417D-27-4	46.50	15.96	10.50	5.41	13.34	2.12	0.48	1.33	0.09	0.15	0.03	4.40	100.3	2.781	2.813	3.2	5.596	3.087	0.28
417D-30-1	45.75	14.89	10.06	5.61	14.96	1.99	0.43	1.20	0.10	0.16	0.03	5.10	100.3	2.833	2.851	1.8	6.037	3.333	0.28
417D-39-4	47.36	17.17	9.92	5.96	13.43	2.05	0.18	1.23	0.09	0.18	0.03	2.60	100.2	2.845	2.866	2.1	6.026	3.382	0.27
417D-45-2	47.62	15.64	11.59	6.57	11.34	2.30	0.28	1.51	0.10	0.18	0.03	3.00	100.2	2.764	2.807	4.3	5.465	3.058	0.27
417D-55-4	48.82	15.09	11.35	6.43	12.42	2.18	0.08	1.53	0.12	0.20	0.04	2.00	100.3	2.834	2.856	2.2	5.931	3.267	0.28
417D-66-3	48.56	16.23	11.36	6.49	11.97	2.18	0.06	1.38	0.09	0.19	0.03	1.60	100.1	2.877	2.891	1.4	6.198	3.392	0.29
418A-15-1	47.81	17.33	10.04	6.12	11.30	2.41	0.10	1.18	0.09	0.11	0.04	3.20	99.7	2.699	2.746	4.8	5.509	3.074	0.27
418A-18-1	48.84	16.67	9.80	6.39	12.83	2.12	0.07	1.09	0.09	0.16	0.03	2.10	100.2	2.854	2.871	1.7	6.189	3.447	0.28
418A-28-1	45.75	17.76	8.90	5.79	12.35	2.07	0.84	0.95	0.09	0.14	0.03	5.60	100.3	2.692	2.718	2.7	5.555	2.992	0.30
418A-37-1	46.11	18.15	9.60	5.68	6.57	1.95	2.77	1.25	0.10	0.07	0.04	8.00	100.3	2.531	2.572	4.0	4.678	2.468	0.31
418A-44-1	47.92	18.06	9.39	5.25	13.57	1.99	0.13	0.99	0.06	0.15	0.04	2.80	100.4	2.793	2.800	2.9	5.881	3.246	0.28
418A-65-1	48.00	16.05	9.98	6.01	13.18	2.22	0.15	1.22	0.10	0.17	0.02	3.10	100.2	2.796	2.817	2.0	5.675	3.170	0.27
418A-77-5	48.43	15.30	10.69	6.91	12.64	2.07	0.07	1.27	0.09	0.18	0.02	2.50	100.2	2.875	2.882	0.7	6.166	3.480	0.27
418A-81-5	49.71	15.24	11.35	7.11	11.77	2.18	0.06	1.38	0.10	0.18	0.03	1.10	100.2	2.947	2.950	0.3	6.368	3.561	0.27
504B-8-3	49.40	16.09	9.61	7.89	12.48	1.92	0.08	0.90	0.06	0.17	0.05	1.60	100.3	2.872	2.898	2.7	5.974	3.326	0.28
504B-41-3	49.28	15.93	9.67	8.95	12.09	1.88	0.04	0.87	0.06	0.16	0.06	1.20	100.2	2.949	2.954	0.5	6.524	3.590	0.28
504B-52-1	49.50	16.10	8.96	8.34	12.45	1.83	0.04	0.83	0.05	0.15	0.05	1.90	100.2	2.909	2.927	1.8	6.120	3.391	0.28
504B-77-3	49.81	14.38	11.08	8.39	11.89	2.12	0.12	1.04	0.06	0.18	0.04	1.10	100.2	2.899	2.924	2.5	6.061	3.382	0.27
504B-88-1	48.81	15.04	9.99	8.59	11.87	1.86	0.04	1.08	0.10	0.24	0.05	2.50	100.2	2.867	2.891	2.4	6.087	3.404	0.27
504B-127-1	49.24	16.04	9.20	9.11	12.54	1.70	0.04	0.81	0.04	0.16	0.06	1.40	100.3	2.970	2.971	0.1	6.508	3.462	0.30
504B-136-1	49.25	16.08	9.35	9.04	12.61	1.71	0.04	0.82	0.06	0.16	0.06	1.10	100.3	2.979	2.981	0.3	6.510	3.368	0.32
801B-40-1	51.31	17.51	6.76	3.69	3.21	2.16	4.71	2.93	0.57	0.08	0.02	7.30	100.3	2.384	2.485	10.1	3.946	1.910	0.35
801C-1-3	47.56	16.39	6.98	3.85	6.36	2.23	4.39	2.75	0.53	0.19	0.03	9.50	100.8	2.428	2.520	6.9	4.058	1.944	0.35
801C-2-1	49.00	17.18	7.55	3.02	2.82	2.29	4.86	3.20	0.59	0.16	0.02	9.10	99.8	2.449	2.536	8.7	4.926	2.211	0.37
801C-5-413	47.73	16.04	9.19	7.35	11.04	2.14	0.15	1.27	0.12	0.15	0.06	4.70	99.9	2.863	2.872	1.0	6.337	3.520	0.28
801C-2-3	46.71	16.09	9.42	5.36	7.40	2.72	2.51	2.51	0.46	0.17	0.02	7.40	100.8	2.619	2.681	6.2	4.929	2.655	0.30

* Fe as Fe_2O_3

MICROCRACK POROSITY: VELOCITY AND INVERSION DATA

In the present study, microcrack porosity was examined in basalts taken from DSDP holes 417A, 417D, 418A, 504B and 483B. These holes were chosen primarily because a significant number of core samples were available from each (Table 1). Three complementary techniques were used to examine microcracks, which will be described briefly. First, unsaturated compressional-wave velocity data as a function of confining pressure were analysed. Velocity increase with confining pressure is mainly caused by the increasing stiffness of the rock mass due to microcrack closure (and/or the increasing contact of asperties on the crack surfaces) (Birch 1960). Thus, by comparing velocities measured at very low confining pressures (10 MPa) to those measured at high confining pressures (where most cracks are closed), a rough estimate of microcrack porosity can be obtained for a given core (e.g. O'Connell & Budiansky 1974; Kowallis & Wang 1983). In particular, rocks with small values of the ratio of low-pressure velocity to high-pressure velocity probably contain more microcrack porosity than samples with higher values of this ratio (e.g. Nur & Simmons 1970; O'Connell & Budiansky 1974). Dry compressional-wave velocities only were chosen for analysis since these data are generally more reliable at low pressures than saturated velocities. Additionally, saturation of heavily altered samples may cause changes in the actual matrix of the basalt that would obscure the influence of microcracks on velocity (e.g. Carlson & Herrick 1990). The second microcrack analysis technique involved using the measured velocity–pressure curves and the Cheng–Toksoz (1979) inversion scheme to estimate the pore-aspect-ratio spectra of the basalts. Lastly, SEM images of polished thin sections were used to obtain qualitative estimates of microcrack porosity that could be compared to the results of the inversion and velocity analysis. A brief description of the Cheng–Toksoz inversion scheme will be given before examining the results of the microcrack study in detail.

The inversion algorithm developed by Cheng & Toksoz (1979) is based on the effective medium theory of Kuster & Toksoz (1974). For a given rock sample, using measured V_p and V_s as a function of confining pressure, estimates of the elastic moduli of the matrix and the pore-filling material, and total sample porosity, the Cheng–Toksoz program solves for the distribution of total porosity among pores of various aspect ratios, or the pore-aspect-ratio spectrum, at atmospheric pressure (a spherical pore has an aspect ratio of 1; thin cracks have very small aspect ratios). The Cheng–Toksoz code is a standard linearized inversion; an initial guess at the pore-aspect-ratio spectrum is iteratively improved by minimizing the difference between calculated and observed velocities. Aspect ratios to solve for are entered into the program. Since it is unrealistic to suggest that the exact pore aspect ratios of a given rock can be specified given their complex structure (e.g. Burns, Cheng & Wilkens 1990), the pore aspect ratios listed in Table 3 were used in all inversions, forcing the program to apportion porosity among them. In general, only those pores that close over the pressure range of interest are resolved well by the program (closure of a given aspect-ratio pore results in a significant increase in elastic moduli; pores that remain open have relatively little effect). Among the samples studied, pores of aspect ratio 0.0005, 0.001 and 0.002 (occasionally 0.003 and 0.004) close over the pressure range 10–200 MPa. Pores of higher aspect ratio (e.g. 0.1 and 1.0) act mostly as 'dumps' so that calculated porosity equals true porosity.

Dry velocity data were used in the inversions for the reasons given above. In addition, the crack-closure calculations used in the inversion require the static bulk modulus of the sample

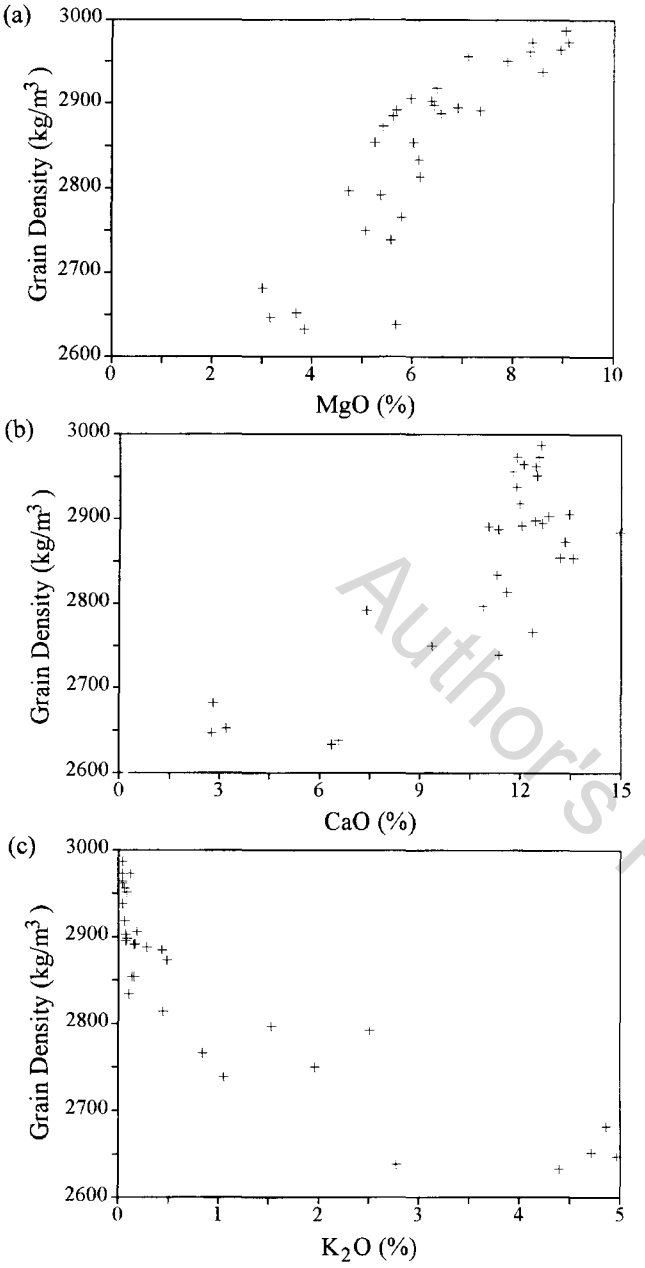

Figure 6. Grain densities plotted as a function of weight per cent MgO (a), CaO (b) and K_2O (c) content.

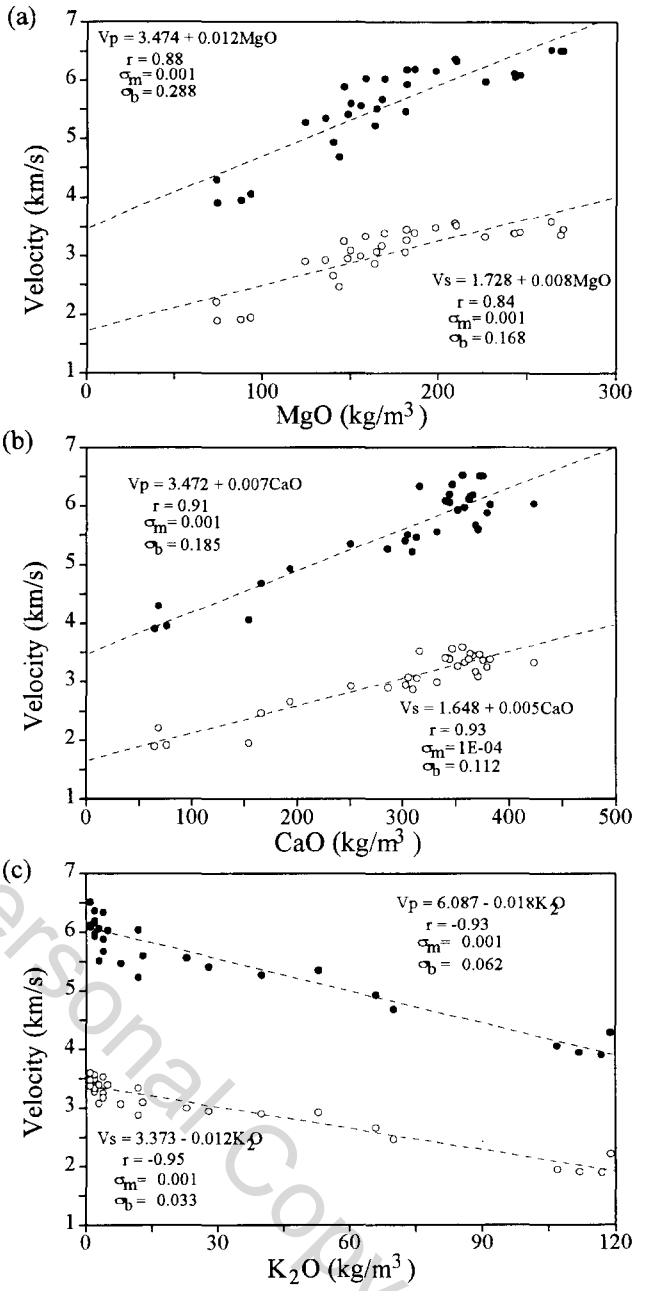

Figure 7. Compressional- (black dots) and shear-wave (open dots) velocities as a function of MgO (a), CaO (b) and K_2O (c) content. Least-squares lines through the data and correlation coefficients are also shown.

of interest as a function of pressure. These data are generally unavailable (e.g. Cheng & Toksoz 1979; Kowallis & Wang 1983) but dry effective moduli more closely approximate the static moduli than wet bulk moduli (Cheng & Toksoz 1979).

The results of a typical inversion run are given in Fig. 10 for a Hole 417D basalt. The fit of the observed to the calculated velocities is quite good for this sample (Fig. 10a). The 'stepped' nature of the calculated velocities is due to the fact that we are solving for a finite number of aspect ratios; when cracks having a specific aspect ratio close, a large jump in calculated elastic moduli, and hence velocities, occurs. The calculated pore-aspect-ratio spectrum and estimated standard deviations are given in Fig. 10(b). For this sample pores of aspect ratios 0.0005, 0.001, 0.002, and 0.003 close over the pressure range 10–200 MPa and are thus well resolved.

As a last point it should be emphasized that the results of the Cheng–Toksoz inversion are model-dependent (e.g. Cheng & Toksoz 1979) and thus do not necessarily represent the 'true' pore structure of a rock. The inversion is used in the present study only to estimate relative differences in microcrack porosity from sample to sample. In particular, to avoid over-interpreting the inversion results, the fractional porosities assigned by the program to pores of aspect ratios 0.0005, 0.001 and 0.002 are summed for each basalt and referred to as 'inversion data' in the following discussion.

In Fig. 11, total measured porosity, saturated V_p and V_s (200 MPa), dry V_p (10 and 200 MPa), the ratio V_p (10 MPa,

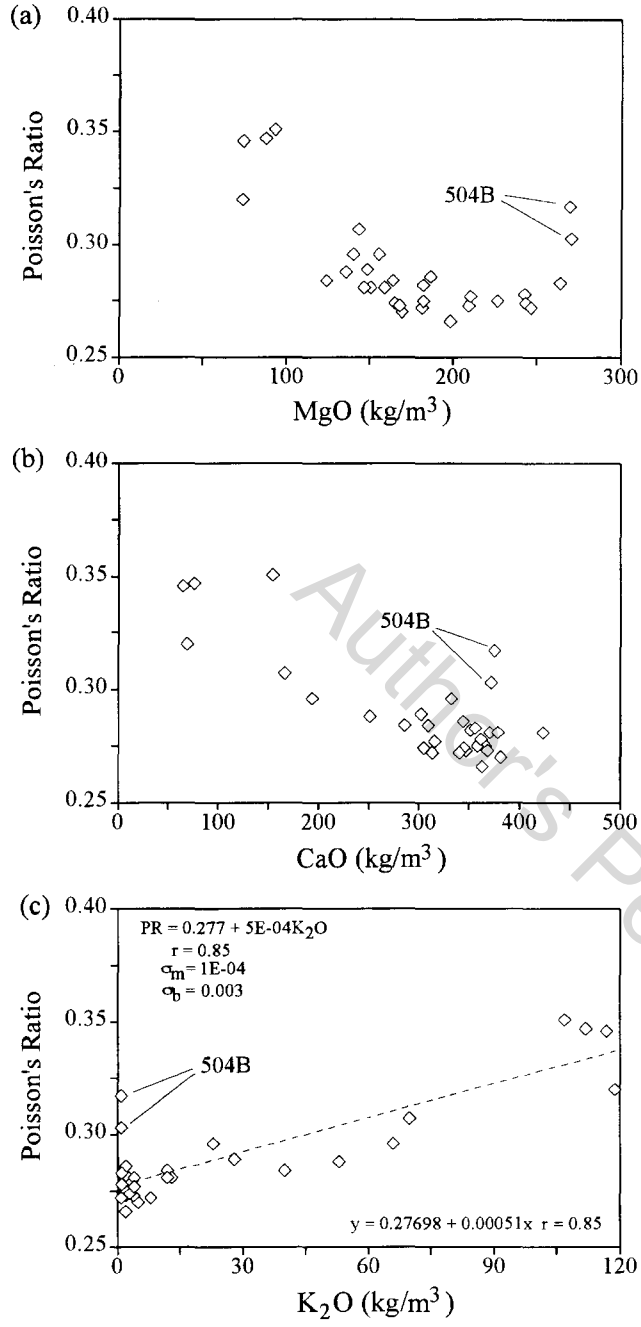

Figure 8. Poisson's ratio as a function of MgO (a), CaO (b) and K_2O (c) content. Least-squares lines through the data and correlation coefficients are also shown. 'Deep' hole 504B samples labelled (see text).

dry)/V_p (200 MPa, dry), and inversion data have been plotted as a function of depth for samples from Hole 417A. A simple stratigraphic column for Hole 417A (Donnelly *et al.* 1980) is included for reference. Velocities of the shallow samples are low due to alteration and relatively high porosities. Note that samples with low V_p ratios generally exhibit greater amounts of microcrack porosity as identified by the inversion, as would be expected.

Similar data for Hole 417D, which penetrated 350 m of pillow basalts and massive flows (Donnelly *et al.* 1980) are presented in Fig. 12. Samples from the upper massive flows are less porous than the samples from the surrounding pillows;

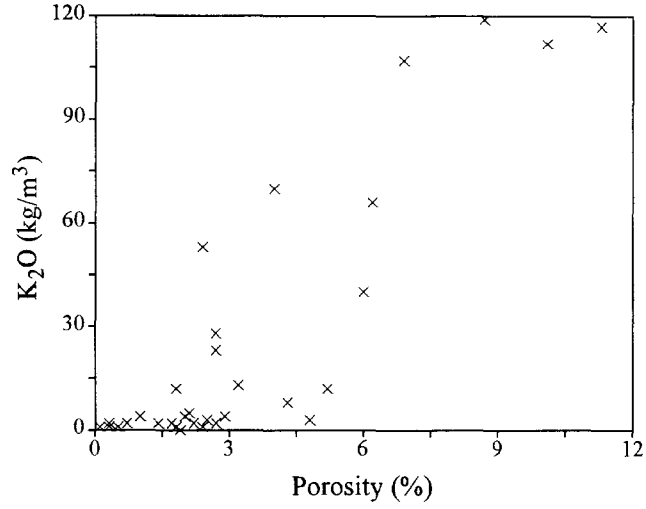

Figure 9. Sample K_2O content plotted as a function of porosity.

Table 3. Pore aspect ratios solved for using Cheng–Toksoz inversion.

1.0
0.1
0.005
0.004
0.003
0.002
0.001
0.00005

otherwise there are no significant changes in total porosity with depth. However, microcrack porosity, as identified through the inversion data and V_p ratio, is significantly higher in the upper massive flows relative to the surrounding pillow units (note in particular the massive unit at approximately 425 mbsf). In addition, pillow basalts from the deeper portions of 417D apparently contain more microcrack porosity than shallow pillow samples.

Total sample porosity in Hole 418A (Fig. 13) decreases with depth. The saturated velocities and dry compressional-wave velocities measured at 200 MPa increase with depth while V_p measured at 10 MPa presents a more scattered trend. As in Hole 417D, samples from massive units exhibit less total porosity, but more microcrack porosity than samples taken in pillow intervals (Fig. 13). Beyond this variation between the massive and pillow units, no broad trends in microcrack porosity are observed. In the pillow basalt interval 510–660 mbsf a very slight increase in microcrack porosity with depth is indicated by the V_p ratio data, and to a lesser extent by the inversion data.

Data for Hole 483B are presented in Fig. 14. 11 samples collected from both massive and pillow units over a relatively short depth interval of approximately 140 m were examined. With one exception, basalts from massive units appear to have more microcrack porosity than samples taken from pillow units (Fig. 14), emphasizing the difference between the pillow/massive unit microcrack porosity observed in 417D and 418A.

Lastly, physical properties and inversion data for Hole 504B are presented in Fig. 15. Overall core recovery in this hole was

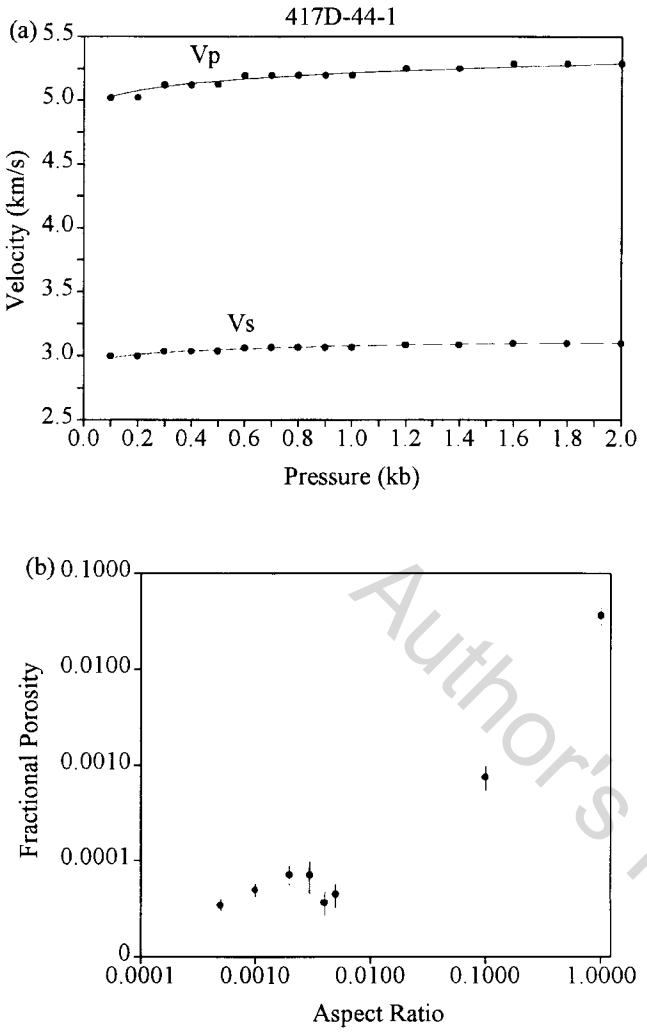

Figure 10. Pore-aspect-ratio inversion results for 417D-44-1 including calculated (symbols) and observed (curves) velocities (a), and calculated pore-aspect-ratio spectrum (b). Bars represent uncertainties in calculated porosities due to variance between calculated and observed velocities.

relatively poor (~25–30 per cent, Anderson *et al.* 1985) compared to 417A, 417D and 418A (~60–70 per cent, Donnelly *et al.* 1980), so only a general stratigraphic column is shown. The majority of the Hole 504B basalts available for study were cored from massive units; the few pillow unit samples are labeled with a 'P'. Fig. 15 indicates that total sample porosity decreases to very small values at depth in Hole 504B (e.g. Salisbury *et al.* 1985). The unsaturated compressional-wave velocity data exhibit contrasting trends. V_p (200 MPa), with a few exceptions, increases with depth. Compressional-wave velocity at 10 MPa decreases with depth, or at least presents a random pattern. Some of the deepest samples exhibit very low 10 MPa velocities. A significant increase of microcrack porosity with increasing sample depth is indicated by the inversion and by V_p ratio data.

A few general conclusions can be drawn from Figs 11–15. In most of the DSDP holes for which significant penetration was achieved (i.e. 417D, 418A, 504B), total sample porosity decreases with depth. However, in the massive basalts of 504B and the pillow basalts of 417D, microcrack porosity apparently increases with increasing sample depth. Least-squares lines fitted to the inversion data of these holes (omitted for clarity) have correlation coefficients of 0.45 and 0.74, respectively. Basalt samples from massive units in general contain more microcrack porosity than samples taken from pillow intervals (Table 4). This is particularly apparent in the Hole 483B data (Fig. 14). Before attempting to explain these trends, it is necessary to examine SEM images of the basalts to determine the origin of the open microcracks.

MICROCRACK POROSITY: SEM IMAGING

To supplement the findings of the velocity–pressure analysis and the inversion, scanning electron microscope studies of cores from Holes 417A, 417D, 418A, 504B and 483B were undertaken. Polished thin sections were made from slabs cut from core samples using a diamond-tipped saw blade that imparted minimal vibration to the samples. Original core end material was available for most of the 418A, 483B and 504B cores. Due to a lack of sample material for Holes 417A and 417D, it was necessary to cut thin-section samples after the cores had been subjected to pressure runs. The effects of this pressure cycling are believed to be minimal and restricted to the crushing of asperities on very low-aspect-ratio cracks, which close over the pressure range 10–200 MPa (e.g. Kranz 1983). All core material was impregnated with low-temperature epoxy prior to polishing to minimize possible damage to the sections induced by this process. It should be acknowledged, however, that cracks in clays observed in the images discussed below could be due to the multiple episodes of sample saturation and drying.

10 to 15 representative basalts were chosen for study from each of holes 417D, 418A and 504B; five were analysed from 417A and 483B. Three sites, chosen randomly, were examined on each polished thin section using the SEM at 100×, 200×, 500×, 1000× and occasionally 2000× magnification. Digital images were collected at each site. Minerals were identified using tone contrasts, optical petrography (when possible), X-ray diffraction, and spot checking using a Cameca SX-50 microprobe. Image processing was confined to adjusting the intensity levels to maximize the contrast between pore space and the surrounding grains.

In the present study the SEM images are used in a qualitative manner to supplement the velocity–pressure and inversion data. In addition, it must be pointed out that while the Cheng–Toksoz inversion program can only accurately resolve cracks with aspect ratios of 0.003 and less, cracks with aspect ratios less than approximately 0.005 cannot usually be clearly observed with the SEM (e.g. Kowallis, Roeloffs & Wang 1982). Thus, the resolution ranges of the two techniques do not overlap.

Sealed microcracks are observed in almost every sample using the petrographic and scanning electron microscopes. Cracks are commonly filled with clays (primarily smectite), calcite, iron oxides/hydroxides, pyrite and chlorite in the deeper Hole 504B samples. Some representative examples of crack sealing will be shown in the following figures. Fig. 16 shows clay-filled cracks cutting through a plagioclase crystal in sample 417D-33-2. A nice example of a smectite/calcite-filled crack cutting through a large plagioclase phenocryst in 417D-66-3 is shown in Fig. 17. Although it is not totally clear from the image, smectite fills every crack except those labelled

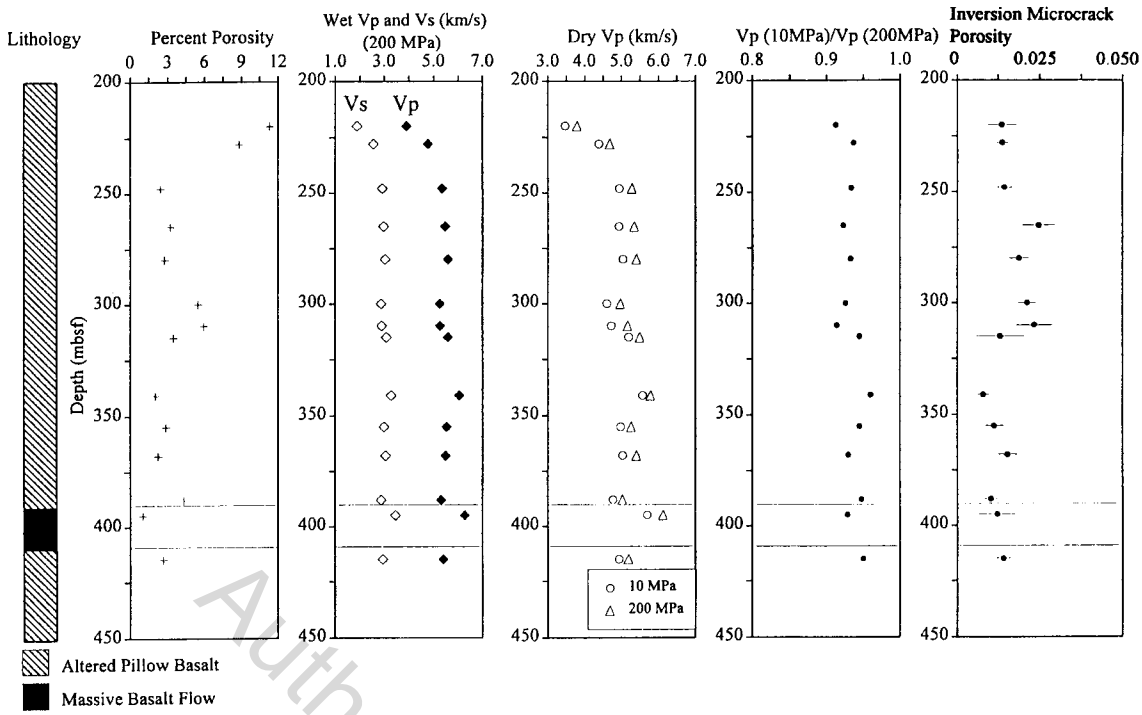

Figure 11. Physical property data for hole 417A samples as a function of depth including total porosities, saturated V_p and V_s, unsaturated V_p, ratio of 10 to 200 MPa compressional-wave velocities (unsaturated), and porosity (from inversions) in pores of aspect ratios 0.0005, 0.001 and 0.002. Lithologic column included for reference (Donnelly *et al.* 1980).

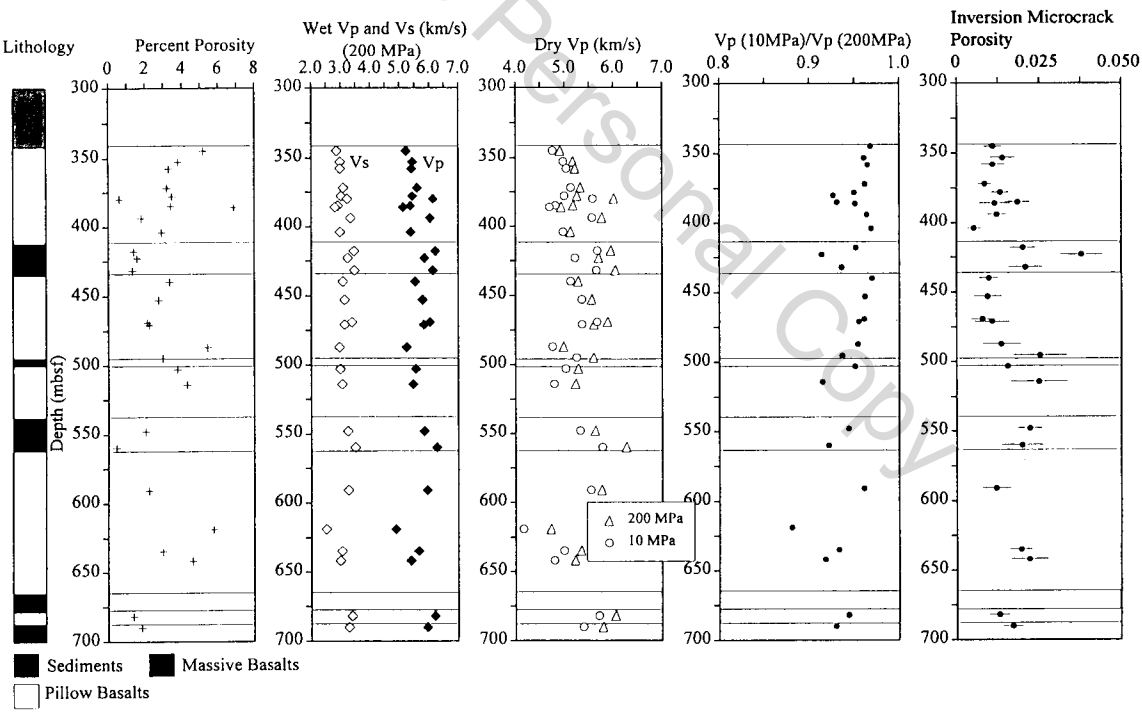

Figure 12. Physical property data for hole 417D samples as a function of depth including total porosities, saturated V_p and V_s, unsaturated V_p, ratio of 10 to 200 MPa compressional-wave velocities (unsaturated), and porosity (from inversions) in pores of aspect ratios 0.0005, 0.001 and 0.002. Lithologic column included for reference (Donnelly *et al.* 1980).

with an 'm' (discussed below). The groundmass in this sample also shows some alteration to clay minerals.

Good examples of crack sealing are generally not as abundant in SEM images collected from shallow Hole 504B samples. However, samples taken from the transition zone and sheeted dyke section are generally marked by pervasive crack filling by clays (primarily smectite) and chlorite. Some of the best examples, observed in sample 504B-127-1, are shown in Fig. 18.

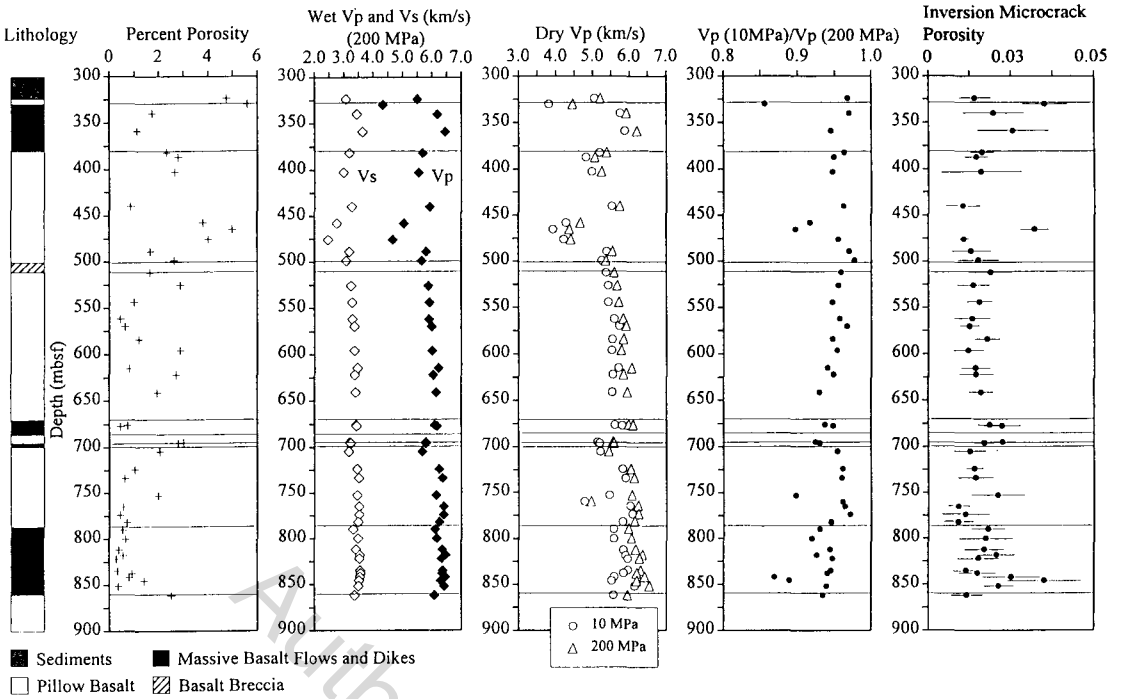

Figure 13. Physical property data for hole 418A samples as a function of depth including total porosities, saturated V_p and V_s, unsaturated V_p, ratios of 10 to 200 MPa compressional-wave velocities (unsaturated), and porosity (from inversions) in pores of aspect ratios 0.0005, 0.001 and 0.002. Lithologic column included for reference (Donnelly *et al.* 1980).

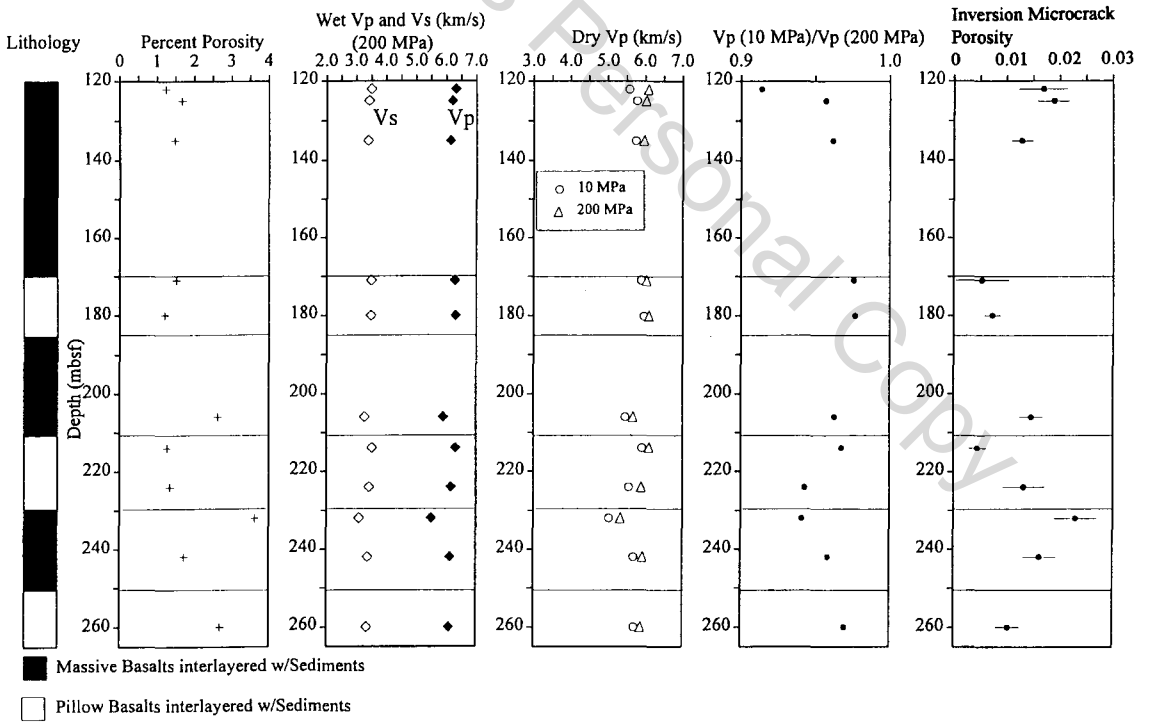

Figure 14. Physical property data for hole 483B samples as a function of depth including total porosities, saturated V_p and V_s, unsaturated V_p, ratio of 10 to 200 MPa compressional-wave velocities (unsaturated), and porosity (from inversions) in pores of aspect ratios 0.0005, 0.001 and 0.002. Lithologic column included for reference (Lewis *et al.* 1983).

In Fig. 18(b), note the delicate bridges found between the two plagioclase crystals at 2000 × magnification.

Isolated cracks and pores that have been bridged or 'healed' by late crystallization of plagioclase and/or pyroxene (e.g. Brace *et al.* 1972) but not sealed by secondary minerals are also observed in the sample suite; some of these features can be seen in the image of 417D-33-2 (Fig. 16, labelled 'h'). Partially healed cracks are commonly observed in holocrystal-

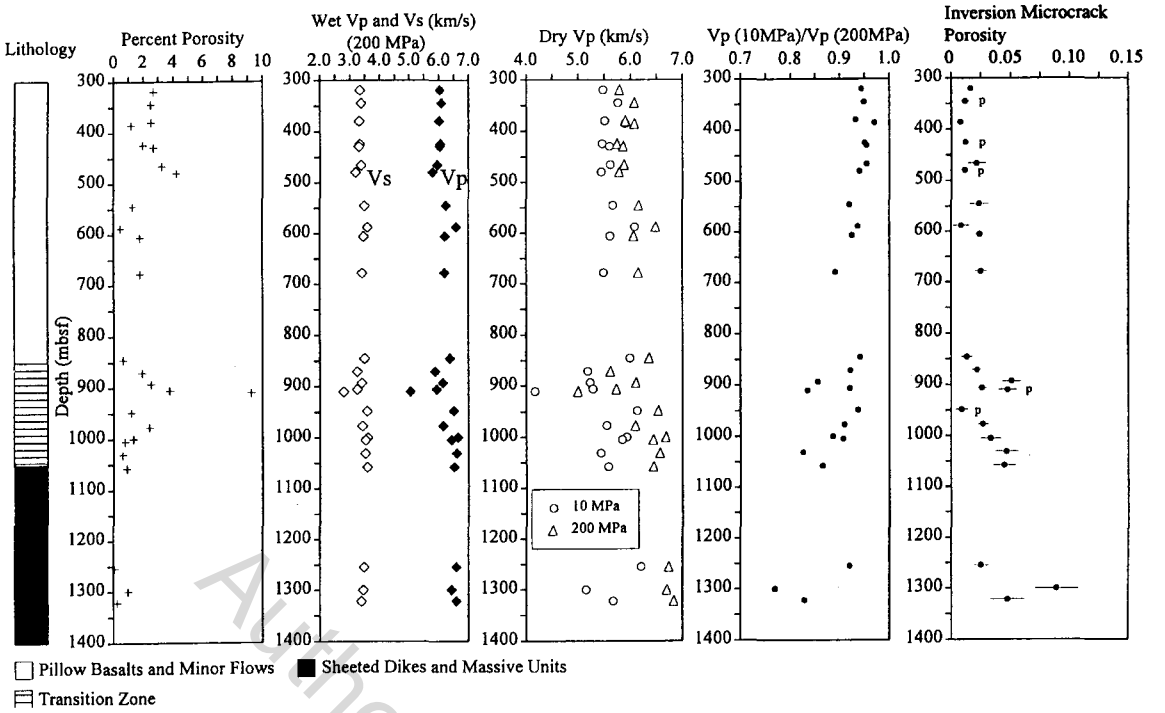

Figure 15. Physical property data for hole 504B samples as a function of depth including total porosities, saturated V_p and V_s, unsaturated V_p, ratio of 10 to 200 MPa compressional-wave velocities (unsaturated), and porosity (from inversions) in pores of aspect ratios 0.0005, 0.001 and 0.002. 'P' indicates pillow basalt sample. Lithologic column included for reference (Anderson *et al.* 1985).

Table 4. Average V_p ratio and fractional microcrack porosity data for pillow (p) and massive (m) basalts of holes 417D, 418A and 483B.

		V_p ratio	Microcrack porosity
417D	p	0.948 ± 0.022	1.33E−04 ± 4.85E−05
	m	0.934 ± 0.013	2.34E−04 ± 6.90E−05
418A	p	0.949 ± 0.020	1.49E−04 ± 4.63E−05
	m	0.927 ± 0.031	2.06E−04 ± 6.65E−05
483B	p	0.969 ± 0.015	8.16E−05 ± 3.60E−05
	m	0.949 ± 0.019	1.71E−04 ± 3.50E−05

line basalts from massive flows and dykes and can take the form of isolated intracrystalline pore spaces (e.g. Fig. 16) or possibly grain-boundary cracks between plagioclase and pyroxene.

The sealed and partially healed microcracks shown in Figs (16)–(18) were present *in situ* in these basalts. However, very low-aspect-ratio microcracks with sharply tapered ends commonly observed at high magnifications (500–1000 ×) were certainly introduced sometime during the drilling and core-recovery process (e.g. Wang & Simmons 1978; Kowallis & Wang 1983; Kranz 1983). Some of these thin microcracks (labelled as 'm' in the figures) are seen branching off the sealed crack in Fig. 17. Man-made cracks are also observed in the large pyroxene crystal and interstitial clay/chlorite shown in Fig. 18. Generally these thin microcracks are most abundant in the holocrystalline, coarse-grained basalts of massive flow units and dykes as well as in the phenocrysts of phyric samples taken from pillow units. They take the form of grain-boundary (Fig. 19) and intracrystalline cracks (Fig. 20).

High-magnification SEM images of the glassy/cryptocrystalline groundmasses of phyric samples provide a strong contrast to the coarse-grained basalt images. Very few, if any, open microcracks are observed. This is nicely illustrated by an image of a Hole 418A pillow basalt sample shown in Fig. 21.

DISCUSSION

Although polished-thin-section preparation (including cutting of slabs from core ends) may introduce some of the observed open microcracks, the use of diamond-tipped saw blades and the impregnation of samples with low-temperature epoxy before polishing minimize potential preparation damage. Instead, the fractures were probably caused by stress relief when the samples were removed from *in situ* pressure conditions, an interpretation similar to that of Wang & Simmons (1978) and Kowallis & Wang (1983) for continental drill holes. A basalt core removed from high-effective-pressure conditions at depth and brought to the surface will undergo a slight increase in volume. The crystals in a typical basalt (e.g. plagioclase, pyroxene) have differing compressibilities. Thus, intergranular stresses will be introduced in a core as it undergoes decompression, which can result in stress-relief microcracking. Simple calculations show that the approximate confining pressures at the bases of holes 417D, 418A and 504B (at the end of leg 83) are 70, 75 and 70 MPa, respectively. If atmospheric pore pressure is assumed to exist at depth in these holes, the deepest basalt cores would undergo a 70–75 MPa decrease of confining pressure and a great deal of stress-relief microcracking would be expected. On the other hand, if it is assumed that pore pressures are hydrostatic (that is, pore water is in communication with the overlying column of seawater), relatively small differential pressures of approximately 10 MPa would exist at the base of these holes. This scenario would seem to imply that very little, if any, stress-

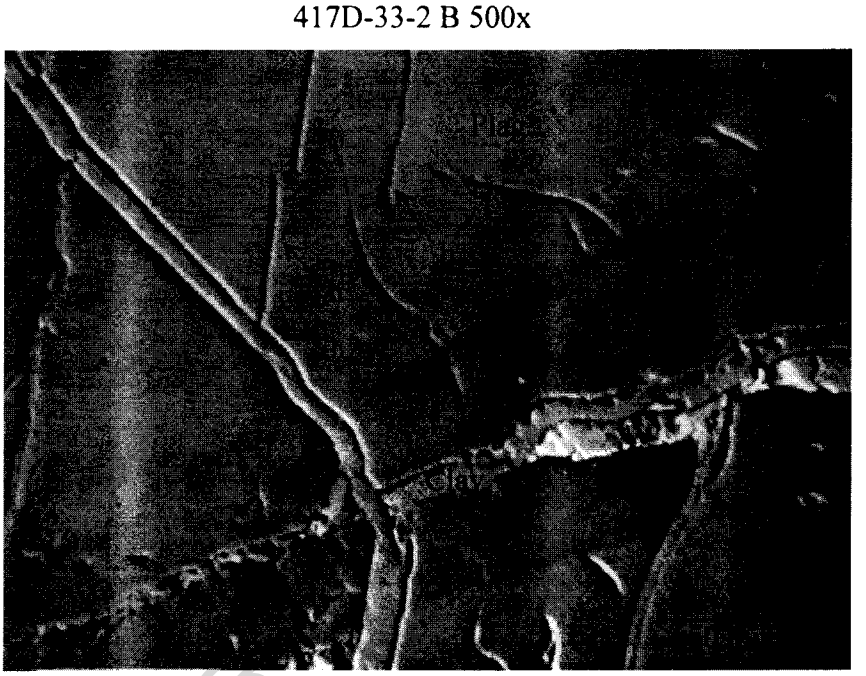

Figure 16. Clay-filled cracks in large plagioclase crystal (417D-33-2). Note abundant partially healed (h) cracks.

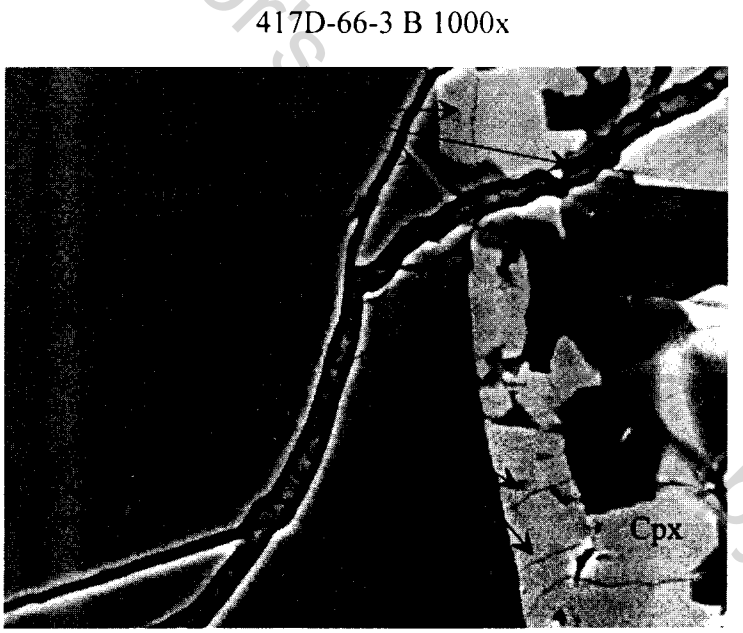

Figure 17. Smectite/calcite-filled crack cutting large plagioclase crystal in 417D-66-3. Note apparent stress-relief cracks (m) in plagioclase and pyroxene.

relief microcracking would occur in deep core samples. It seems unlikely, however, that the permeability of the basalt cores would be high enough (e.g. Christensen & Ramananantoandro 1988) to allow gradual release of pore fluid as external confining pressure was released during core transport to the surface. Trapped pore fluids could thus result in extreme differential pressure conditions being developed during transport, which also could result in microcracking (e.g. Johnston, Fryer & Christensen 1995). In reality, pore-pressure conditions in these holes are relatively unknown (there are some indications of non-hydrostatic pore pressures in the upper volcanic section of 504B, e.g. Anderson *et al.* 1985) and the true situation is probably somewhere between the two extremes described here.

Microcracking could also be introduced in core samples by differential thermal contraction of minerals (or anisotropic differential thermal contraction among different grains of the same mineral) during removal from *in situ* temperature conditions (e.g. Nur & Simmons 1970). Temperature logging of Hole 504B indicated *in situ* temperatures of approximately 160 °C at 1300 mbsf (Becker *et al.* 1985). Considerably less complete logging data for Hole 418A indicated relatively cool

504B-127-1 B 1000x

2000x

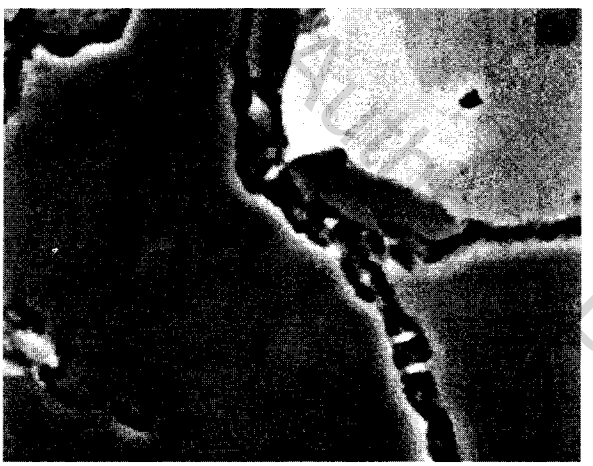

Figure 18. Chlorite-filled microcracks in 504B-127-1. Note small 'bridges' observed in filled crack at 2000× (b) as well as apparent stress-relief microcracks (m) in pyroxene (a).

conditions at depth with a minimum temperature of approximately 25 °C at 800 mbsf (Salisbury *et al.* 1986). Considering that confining pressures at depth in Holes 418A and 504B are roughly equivalent, differential thermal contraction could account for the significant increase in microcracking with depth observed in Hole 504B that is not found in Hole 418A.

The SEM survey summarized above confirms the results of the velocity analysis and the inversion, in that holocrystalline, coarse-grained basalts from massive flows contain more open microcracks than do phyric samples from pillow units (Figs 19 and 21). This difference in microcracking might be explained using basic fracture mechanics. According to Griffith fracture theory, when a material is stressed the stress tends to be concentrated at pre-existing 'flaws' in the material. Flaws can be cracks, grain boundaries, cleavage planes, etc. Stress is concentrated at the tips of these features; the greater the length of the flaw, the greater the stress concentration (Scholz 1990). A coarse-grained rock contains longer flaws in terms of cleavage planes and grain boundaries than a fine-grained sample of the same mineralogy. Thus, greater stress concentrations, and hence greater microcracking (grain boundary, cleavage plane, etc.), would be expected in the coarse-grained basalts upon their removal from *in situ* pressure and temperature conditions than in phyric samples with cryptocrystalline groundmasses. Fig. 19 shows some of the better examples of grain-boundary microcracking in coarse-grained basalts. Although no examples can be found in the SEM images, it should be noted that cracks filled with smectite and chlorite are likely to be 'reactivated' during core recovery due to the weak mechanical strength of these minerals.

An additional factor can also account for greater stress-relief microcracking in coarse-grained basalts: once an intercrystalline or intracrystalline crack begins propagating in a material, grain boundaries and pre-existing cracks can act as barriers to arrest the progress of the crack (this is assuming that the stresses necessary to start the cracking are less than those necessary to propagate it across a boundary) (e.g. Knudsen 1959; Rice 1974; Rong, Xaio-Xin & Hung-Sen 1979; Santarelli

504B-8-3 C 1000x

Figure 19. Probable grain-boundary stress-relief microcracks in 504B-8-3. Note termination of cracks against other cracks.

Figure 20. Stress-relief microcracks in plagioclase phenocryst of 417D-30-1. Note terminations against grain boundaries.

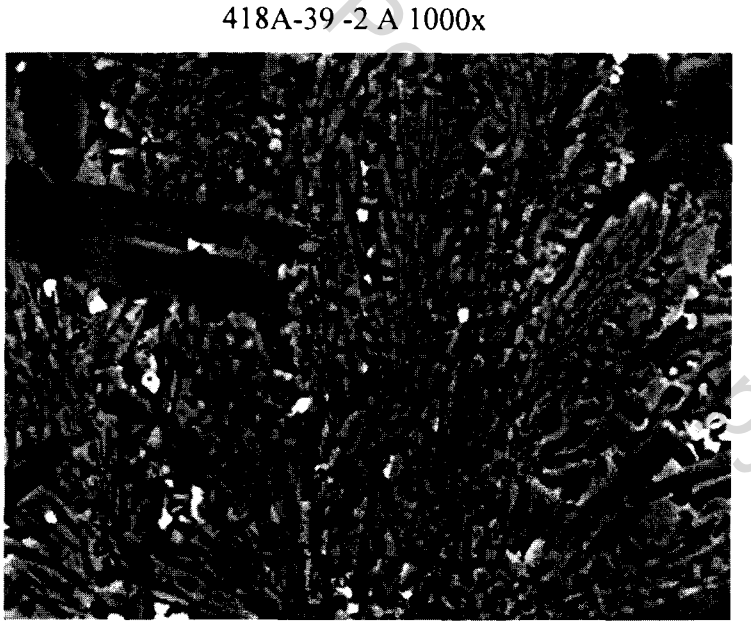

Figure 21. High-magnification images of 418A-39-2 groundmass. Note lack of microcracks.

& Brown 1989). There are more grain boundaries per unit volume in fine-grained basalts than in coarse-grained samples. Thus, if stress relief/thermal contraction microcracking is begun in a phyric basalt with a cryptocrystalline groundmass, it has a greater chance of being halted than in a coarse-grained sample with larger crystals and longer continuous grain boundaries. Many examples of stress-relief microcracks terminating against grain boundaries and other cracks can be seen in Figs 17–20.

Lastly, it should be noted that the stress-relief microcracking observed in DSDP/ODP basalts is apparently not as severe as that observed by Kowallis & Wang (1983) in granitic cores taken from the Illinois deep borehole UPH-3. Among other aspects of their investigation, Kowallis & Wang measured the velocities of four granite cores taken from 696 to 1572 m below the surface (roughly equivalent to *in situ* confining pressures of 20 to 40 MPa). While compressional-wave velocities at 200 MPa were found to increase (6.18 km s^{-1} to 6.61 km s^{-1})

with increasing sample depth, 10 MPa velocities decreased significantly (5.78 km s^{-1} to 4.66 km s^{-1}) (Kowallis & Wang 1983). This corresponds to a decrease of the V_p (10 MPa)/V_p (200 MPa) ratio from 0.93 to 0.70, a more severe decrease than any observed in the present study, where *in situ* confining pressures can range up to 75 MPa. Thus, stress-relief microcracking appears to be much more prominent in the granites studied by Kowallis & Wang (1983) than in the basalts of the present study. In large part, this phenomenon is probably due to the presence of quartz in granite. Quartz has significantly higher compressibility and coefficient of thermal expansion values than other common rock-forming minerals (Table 5) (e.g. Birch 1960; Nur & Simmons 1970). Under the same *in situ* temperature and pressure conditions, stronger intergranular stresses would be introduced in a granite during core recovery than in a basalt.

CONCLUSIONS

In this study the physical properties of a large suite of layer 2 basalts from some important DSDP/ODP holes have been investigated. The focus of this investigation has been on two aspects of layer 2 basalts that have received relatively little attention: microcrack porosity and alteration-related changes in physical properties. Alteration, effectively constrained by sample K_2O content, has been shown to result in lowered velocities and increased Poisson's ratios relative to values for fresh basalts. These findings largely confirm the earlier results of Christensen & Salisbury (1972, 1973), Hart (1973) and Hyndman (1979), with the added benefit of being derived from a large data set.

Porosities and pore aspect ratios of the basalts have been investigated using several complementary techniques. SEM images indicate that natural fractures either healed by late crystallization or sealed by alteration minerals such as smectite and calcite are found throughout the sample suite. Abundant clay- and chlorite-filled microcracks are found in the transition zone and below in Hole 504B. The most significant microcrack porosity trend identified in the basalt suite is attributed to stress relief, which occurred when the original drill cores were removed from *in situ* conditions. Stress-relief microcracking is particularly apparent in the deeper samples from holes 417D and 504B. The relatively severe microcracking observed in coarser-grained basalts is attributed to the large intrinsic 'flaws' in these samples and the fact that decompression-induced stresses become highly concentrated at these features. Thus, fine-grained basalts with micro- or cryptocrystalline groundmasses are apparently not as affected by decompression. This grain-size dependence of stress-relief microcracking has not been recognized previously. Although the results of this study suggest that caution should be exercised in the interpretation of low-pressure laboratory rock-velocity data, stress-relief microcracking in DSDP/ODP basalts may not be as severe as that found in quartz-bearing rocks such as the granitic cores from the Illinois deep borehole examined by Kowallis & Wang (1983).

Table 5. Aggregate compressibilities (β) and coefficients of thermal expansion (α_v, at 20 °C) of some common rock-forming minerals. Data from Simmons & Wang (1971) and Skinner (1963).

	β (Voigt) (Mb^{-1})	β (Reuss) (Mb^{-1})	α_v ($\times 10^{-6}$ °C)
Augite	0.99	1.11	18
Diopside	0.85	0.95	24
Plag. Feldspar	1.35	1.47	13
Microcline	1.677	2.012	–
Oligoclase	1.42	1.648	–
Olivine	0.75	0.78	27
Magnetite	0.62	0.62	–
Calcite	1.26	1.36	–
Pyrite	0.70	0.70	–
Quartz	2.64	2.67	34

ACKNOWLEDGMENTS

Roy Wilkens at the Hawaii Institute of Geophysics provided invaluable assistance in obtaining the SEM images. Reviews by M. Salisbury and R. Carlson greatly improved the manuscript. This work was supported by the Office of Naval Research contract N00014-89-J-1209 and a Purdue Research Foundation Grant.

REFERENCES

Alt, J.C. & Honnorez, J., 1984. Alteration of the upper oceanic crust, DSDP site 417: mineralogy and chemistry, *Contrib. Mineral. Petrol.*, **87**, 149–169.

Alt, J.C., Honnorez, J., Laverne, C. & Emmerman, R., 1986. Hydrothermal alteration of a 1 km section through the upper oceanic crust, Deep Sea Drilling Project Hole 504B: Mineralogy, chemistry, and evolution of seawater-basalt interactions, *J. geophys. Res.*, **91**, 10 309–10 335.

Anderson, R.N., Honnorez, J., Becker, K. *et al.*, 1985. *Init. Repts. DSDP*, **83**, Washington, DC.

Becker, K., Langseth, M.G., Von Herzen, R.P., Anderson, R.N. & Hobart, M.A., 1985. Deep Crustal Geothermal Measurements, Hole 504B, Deep Sea Drilling Project Legs 69, 70, 83, and 92, in *Init. Repts. DSDP*, **83**, pp. 217–248, eds Anderson, R.N., Honnorez, J., Becker, K., *et al.*, Washington, DC.

Berge, P.A., Fryer, G.J. & Wilkens, R.H., 1992. Velocity–porosity relationships in the upper oceanic crust: Theoretical considerations, *J. geophys. Res.*, **97**, 15 239–15 254.

Birch, F., 1960. Velocity of compressional waves in rocks to 10 Kilobars, 1, *J. geophys. Res.*, **65**, 1083–1102.

Brace, W.F., Silver, E., Hadley, K. & Goetze, C., 1972. Cracks and pores: A closer look, *Science*, **178**, 162–164.

Burns, D.R., Cheng, C.H. & Wilkens, R.H., 1990. Sandstone pore aspect ratio spectra from direct observation and velocity inversion, *Int. J. Rock Mech. Min. Sci.*, **27**, 315–323.

Busch, W.H., Castillo, P.R., Floyd, P.A. & Cameron, G., 1992. Effects of alteration on physical properties of basalts from the Pigafetta and East Mariana Basins, in *Proc. ODP, Sci. Results*, **129**, pp. 361–388, eds Larson, R.L., Lancelot, Y., *et al.*, College Station, TX.

Cann, J.R., Langseth, M.G., Honnorez, J., Von Herzen, R.P., White, S.M., *et al.*, 1983. *Init. Repts. DSDP*, **69**, Washington, DC.

Carlson, R.L. & Herrick, C.N., 1990. Densities and porosities in the oceanic crust and their variations with depth and age, *J. geophys. Res.*, **95**, 9153–9170.

Cheng, C.H. & Toksoz, M.N., 1979. Inversion of seismic velocities for the pore aspect ratio spectrum of a rock, *J. geophys Res.*, **84**, 7533–7543.

Christensen, N.I., 1972. Compressional and shear wave velocities at pressures to 10 kilobars for basalts from the East Pacific Rise, *Geophys. J. R. astr. Soc.*, **28**, 425–429.

Christensen, N.I., 1984. Pore pressure and oceanic crustal seismic structure, *Geophys. J. R. astr. Soc.*, **79**, 411–423.

Christensen, N.I., 1985. Measurements of dynamic properties of rocks

at elevated temperatures and pressures, in *Measurements of Rock Properties at Elevated Pressures,* pp. 93–107, eds. Pincus, H.J. & Hoskins, E.R., American Society for Testing and Materials, Philadelphia, PA.

Christensen, N.I. & Ramananantoandro, R., 1988. Permeability of the oceanic crust based on experimental studies of basalt permeability at elevated pressures, *Tectonophysics,* **149,** 181–186.

Christensen, N.I. & Salisbury, M.H., 1972. Sea floor spreading, progressive alteration of layer 2 basalts, and associated changes in seismic velocities, *Earth planet. Sci. Lett.,* **15,** 367–375.

Christensen, N.I. & Salisbury, M.H., 1973. Velocities, elastic moduli, and weathering-age relations for pacific layer 2 basalts, *Earth planet. Sci. Lett.,* **19,** 461–470.

Christensen, N.I. & Salisbury, M.H., 1975. Structure and constitution of the lower oceanic crust, *Rev. Geophys. Space Phys.,* **13,** 57–86.

Christensen, N.I. & Shaw, G.H., 1970. Elasticity of mafic rocks from the Mid-Atlantic Ridge, *Geophys. J. R. astr. Soc.,* **20,** 271–284.

Christensen, N.I., Fountain, D.M. & Stewart, R.J., 1973. Oceanic crustal basement: a comparison of seismic properties of DSDP basalts and consolidated sediments, *Mar. Geol.,* **15,** 215–226.

Donnelly, T.W., Thompson, G. & Robinson, P.T., 1979. Very low temperature hydrothermal alteration of the oceanic crust and the problem of fluxes of potassium and magnesium, in *Deep Drilling Results in the Atlantic Ocean; Ocean Crust,* pp. 369–382, eds. Talwani, M., Harrison, C.G. & Hayes, D.E., *Maurice Ewing Ser., Proc. Symp.* 2, American Geographical Union, Washington, DC.

Donnelly, T., Francheteau, J., Bryan, W., Robinson, P., Flower, M., Salisbury, M., *et al.,* 1980. *Init. Repts. DSDP,* **51,52,53,** Washington, DC.

Ewing, J.I. & Purdy, G.M., 1982. Upper crustal velocity structure in the ROSE area of the East Pacific Rise, *J. geophys. Res.,* **87,** 8397–8402.

Floyd, P.A. & Castillo, P.R., 1992. Geochemistry and petrogenesis of Jurassic ocean crust basalts, site 801, in *Proc. ODP, Sci. Results,* **129,** pp. 361–388, Larson, R.L., Lancelot, Y., *et al.,* College Station, TX.

Fox, P.J., Schreiber, E. & Peterson, J.J., 1973. The geology of the oceanic crust: compressional wave velocities of oceanic rocks, *J. geophys. Res.,* **78,** 5155–5172.

Hart, R.A., 1970. Chemical exchange between sea water and deep ocean basalts, *Earth planet. Sci. Lett.,* **9,** 269–279.

Hart, R.A., 1973. A model for chemical exchange in the basalt–seawater system of oceanic layer 2, *Can. J. Earth Sci.,* **10,** 799–816.

Houtz, R. & Ewing, J., 1976. Upper crustal structure as a function of plate age, *J. geophys. Res.,* **81,** 2490–2498.

Hyndman, R.D., 1979. Poisson's ratio in the oceanic crust—a review, *Tectonophysics,* **59,** 321–333.

Hyndman, R.D. & Drury, M.J., 1976. The physical properties of oceanic basement rocks from deep drilling on the mid-Atlantic ridge, *J. geophys. Res.,* **81,** 4042–4052.

Jacobsen, R.S., 1992. Impact of crustal evolution on changes of the seismic properties of the uppermost ocean crust, *Rev. Geophys.,* **30,** 23–42.

Johnson, H.P. & Semyan, S.W., 1994. Age variation in the physical properties of oceanic basalts: Implications for crustal formation and evolution, *J. geophys. Res.,* **99,** 3123–3134.

Johnston, J.E., Fryer, G.J. & Christensen, N.I., 1995. Velocity–porosity relationships of basalts from the East Pacific Rise, in *Proc. ODP, Sci. Results,* **142,** pp. 51–60, eds Batiza, R., Storms, M.A. & Allan, J.F., College Station, TX.

Kowallis, B.J. & Wang, H.F., 1983. Microcrack study of granitic cores from Illinois Deep Borehole UPH 3, *J. geophys. Res.,* **88,** 7373–7380.

Kowallis, B.J., Roeloffs, E.A. & Wang, H.F., 1982. Microcrack studies of basalts from the Iceland Research Drilling Project, *J. geophys. Res.,* **87,** 6650–6656.

Knudsen, F.P., 1959. Dependence of mechanical strength of brittle polycrystalline specimens on porosity and grain size, *J. Am. ceramic Soc.,* **42,** 376–388.

Kranz, R.L., 1983. Microcracks in rocks: A review, *Tectonophysics,* **100,** 449–480.

Kuster, G.T. & Toksoz, M.N., 1974. Velocity and attenuation of seismic waves in two-phase media, Part I—theoretical formulations, *Geophysics,* **39,** 587–606.

Lancelot, Y., Larson, R., *et al.,* 1990. *Proc. ODP, Init. Repts.,* **129,** College Station, TX.

Lewis, B.T.R., Robinson, P., *et al.,* 1983. *Init. Repts. DSDP,* **65,** Washington, DC.

Moos, D., Pezard, P. & Lovell, M., 1990. Elastic wave velocities within oceanic layer 2 from sonic full waveform logs in Deep Sea Drilling Project Holes 395A, 418A, and 504B, *J. geophys. Res.,* **95,** 9189–9207.

Nur, A. & Simmons, G., 1970. The origin of small cracks in igneous rocks, *Int. J. Rock Mech. Min. Sci.,* **7,** 307–314.

O'Connell, R.J. & Budiansky, B., 1974. Seismic velocities in dry and saturated cracked rocks, *J. geophys. Res.,* **79,** 5412–5427.

Rice, R.W., 1974. Fractographic identification of strength controlling flaws and microstructure, in *Fracture Mechanics of Ceramics,* pp. 323–345, eds Bradt, R.C., Hasselman, P.P.H. & Lange, F.F., Plenum Press, New York, NY.

Rong, C., Xaio-Xin, Y. & Hung-Sen, X., 1979. Studies of the fracture of gabbro, *Int. J. Rock Mech. Min. Sci.,* **16,** 187–193.

Salisbury, M.H. & Christensen, N.I., 1973. Progressive weathering of submarine basalts with age: further evidence of sea-floor spreading, *Geology,* **1,** 63–64.

Salisbury, M.H., Christensen, N.I., Becker, K. & Moos, D., 1985. The velocity structure of layer 2 at Deep Sea Drilling Project Site 504 from logging and laboratory experiments, in *Init. Repts. DSDP,* **83,** pp. 529–539, eds Anderson, R.N., Honnorez, J., Becker, K., *et al.,* Washington, DC.

Salisbury, M.H., Scott, J.H., Aurox, C.A., *et al.,* 1986. *Proc., Initial Repts. (Pt. A), Ocean Drilling Program,* **102,** College Station, TX.

Salisbury, M.H. *et al.,* 1988. Old oceanic crust: Synthesis of logging, laboratory, and seismic data from Leg 102, in *Proc. Ocean Drilling Prog., Scientific Results,* **102,** pp. 155–175, eds Salisbury, M.H., Scott, J.H., *et al.,* College Station, TX.

Santarelli, F.J. & Brown, E.T., 1989. Failure of three sedimentary rocks in triaxial and hollow cylinder compression tests, *Int. J. Rock Mech. Min. Sci.,* **26,** 401–413.

Scholz, C.H., 1990. *The Mechanics of Earthquakes and Faulting,* Cambridge University Press, New York, NY.

Schreiber, E. & Fox, P.J., 1976. Compressional wave velocities and mineralogy of fresh basalts from the FAMOUS area and the Oceanographer fracture zone and the texture of Layer 2a of the oceanic crust, *J. geophys. Res.,* **81,** 4071–4076.

Simmons, G. & Wang, H., 1971. *Single Crystal Elastic Constants and Calculated Aggregate Properties,* MIT Press, Cambridge, MA.

Skinner, B.J., 1963. Thermal expansion, in *Handbook of Physical Constants,* ed. Clark, S.P., *Geol. Soc. Am. Mem,* **97,** 75–96.

Vera, E.E. & Mutter, J.C., 1988. Crustal structure in the ROSE area of the East Pacific Rise: one dimensional travel time inversion of sonobuoys and expanded spread profiles, *J. geophys. Res.,* **93,** 6635–6648.

Wallick, B.P., Christensen, N.I. & Ballotti, D.M., 1990. High pressure velocity measurements of Jurassic basalt, Leg 129, in *Proc. ODP, Sci. Results,* **129,** pp. 501–506, eds Larson, R.L., Lancelot, Y., *et al.,* College Station, TX.

Wang, H.F. & Simmons, G., 1978. Microcracks in crystalline rock from 5.3 km depth in the Michigan Basin, *J. geophys. Res.,* **83,** 5849–5856.

Wilkens, R.H., Fryer, G.J. & Karsten, J., 1991. Evolution of porosity and seismic structure of the upper oceanic crust: Importance of aspect ratios, *J. geophys. Res.,* **96,** 17981–17995.